Yokoo *et al. Earth, Planets and Space* (2019) 71:12
https://doi.org/10.1186/s40623-019-0993-y

Earth, Planets and Space

FULL PAPER Open Access

Monochromatic infrasound waves observed during the 2014–2015 eruption of Aso volcano, Japan

Akihiko Yokoo[1*], Kyoka Ishii[1,2], Takahiro Ohkura[1] and Keehoon Kim[3]

Abstract

Monochromatic infrasound waves are scarcely reported volcanic infrasound signals. These waves have the potential to provide constraints on the conduit geometry of a volcano. However, to further investigate the waves scientifically, such as how the conduit shape modulates the waveforms, we still need to examine many more examples. In this paper, we provide the most detailed descriptions of these monochromatic infrasound waves observed at Aso volcano in Japan. At Aso volcano, a 160-day-long magmatic eruption occurred in 2014–2015 after a 20-year quiescent period. This eruption was the first event that we could monitor well using our infrasound network deployed around the crater. Throughout the entire eruption period, when both ash venting and Strombolian explosions occurred, monochromatic infrasound waves were observed nearly every day. Although the peak frequency of the signals (0.4–0.7 Hz) changed over time, the frequency exhibited no reasonable correlation with the eruption style. The source location of the signals estimated by considering topographic effects and atmospheric conditions was highly stable at the active vent. Based on the findings, we speculate that these signals were related to the resonant frequencies of an open space in the conduit: the uppermost part inside the vent. Based on finite-difference time-domain modeling using 3-D topographic data of the crater during the eruption (March 2015), we calculated the propagation of infrasound waves from the conduit. Assuming that the shape of the conduit was a simple pipe, the peak frequency of the observed waveforms was well reproduced by the calculation. The length of the pipe markedly defined the peak frequency. By replicating the observed waveform, we concluded that the gas exhalation with a gas velocity of 18 m/s occurred at 120 m depth in the conduit. However, further analysis from a different perspective, such as an analysis of the time difference between the arrivals of infrasound and seismic waves, is required to more accurately determine the conduit parameters based on observational data.

Keywords: Monochromatic infrasound wave, Aso volcano in Japan, The 2014–2015 eruption, Air resonance in the conduit

Introduction

Erupting volcanoes are principal sources of infrasound waves. Previous work has shown that infrasound waves can be used to study and monitor volcanoes (Fee and Matoza 2013; Johnson and Ripepe 2011). Infrasound waves observed in volcanic settings are currently commonly used to aid in the monitoring of volcanic activity and the mitigation of hazards posed by eruptions (McNutt et al. 2016). Additionally, infrasound-based studies can provide more valuable information about eruption dynamics that can be used to develop quantitative models of eruptions. Kim et al. (2015) presented a waveform inversion technique that uses infrasound data to estimate the volume flux during an eruption. Fee et al. (2017b) demonstrated that the inversion method showed sufficient promise for the quantitative characterization of eruption parameters, volume and mass flow rates, taking the Vulcanian eruptions at Sakurajima volcano as an example.

*Correspondence: yokoo.akihiko.5a@kyoto-u.ac.jp
[1] Aso Volcanological Laboratory, Institute for Geothermal Sciences, Kyoto University, 3028 Sakanashi, Aso, Kumamoto 869-2611, Japan
Full list of author information is available at the end of the article

Infrasound tremor occurring during eruptions is one type of infrasound waves recorded at volcanoes. Such tremor is generally observed during large Plinian-style eruptions with sustained ash plumes (Fee et al. 2017a). These infrasound waves have been studied by comparing them with jet noises produced from turbulent flows (Matoza et al. 2009). In contrast to those observed in large-scale eruptions, infrasound tremor in small-scale open-vent eruptions has infrequently been observed at only a few volcanoes, namely Hawaii, Villarrica, Sakurajima, and Etna volcanoes. The frequency of the tremor shows a monochromatic nature, with a significant peak occurring at a low frequency. The source mechanisms of the tremor have been proposed to be the resonance of the topographic cavity above the lava lake (Fee et al. 2010), the resonance of the air column at the uppermost end of the conduit (Goto and Johnson 2011; Johnson et al. 2018a; Spina et al. 2015), or the resonance of the ash-gas column above the fragmentation front in the conduit during ash-gas ejection (Yokoo et al. 2008). Another potential source of such infrasound signals was also proposed to be the direct relation of the flow dynamics of gas bubbles during their ascent in the magma column (Ripepe et al. 2010). The source mechanisms have not yet been conclusively defined.

Monochromatic infrasound tremor can be a good indicator of volcanic activity. By monitoring the frequency content and damping characteristics of monochromatic infrasound waves, Johnson et al. (2018a) succeeded in detecting the rising level of the lava lake in the crater of Villarrica volcano preceding its significant 2015 eruption. However, little is known about the capability of using these signals, mainly because such tremor has not been well reported. To further investigate the source process of monochromatic infrasound waves during a volcanic eruption, we still need to examine many more examples.

Here, we report the infrasound signals observed during the 2014–2015 eruption of Aso volcano in Japan (Fig. 1). The infrasound signals at Aso volcano stand out because they had an extraordinarily low-frequency peak (~ 0.5 Hz) and lasted for more than minutes to hours and days. In addition to presenting the characteristic properties of the observed infrasound waves, we also present a preliminary elucidation of these datasets based on the numerical calculations of air resonance inside the conduit.

Eruptions of Aso volcano in 2014–2015

Aso volcano, which is an active volcano in Japan, is located on Kyushu island, SW Japan (Fig. 1a). At an eruptive vent inside its summit crater "Nakadake-1st-crater" (cross in Fig. 1c), the most recent magmatic eruption of Aso volcano began on November 25, 2014 (the dates and times reported in this paper are all in Japan local time, i.e., + 9 h from UT) after 20 years of quiescence (Yokoo

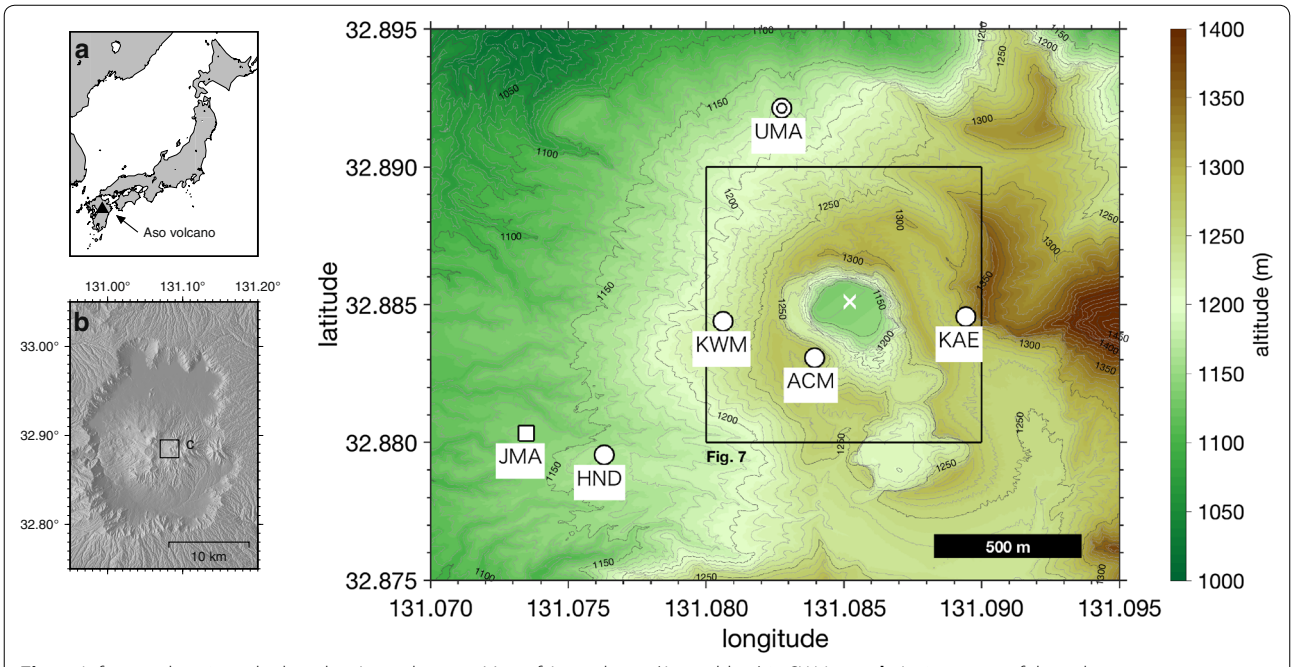

Fig. 1 Infrasound stations deployed at Aso volcano. **a** Map of Aso volcano (Aso caldera) in SW Japan. **b** Active crater of the volcano (Nakadake-1st-crater) is located at the center of the caldera. **c** Infrasound stations indicated by circles are installed around the active crater, where a cross marks the eruptive vent. The UMA station (double circle) is also equipped with a broadband seismometer. A square indicates a weather station of JMA

and Miyabuchi 2015). The 2014–2015 eruption was characterized by a combination of ash venting and frequent Strombolian explosions (Fig. 2). A total of 2.1×10^6 tons of ash was ejected over six months of activity (Miyabuchi et al. 2018), corresponding to 0.8 km^3 DRE magma. This amount of magma was one order of magnitude smaller than the amount of ash produced by the 1989–1991 eruptions (Ono et al. 1995). The size of the vent we measured from the SSW crater rim in the first few days of the 2014–2015 eruption was approximately 10 m in diameter (Fig. 3). This diameter increased rapidly during the first 1.5 months to 45 m and then gradually increased. The vent eventually reached $\sim$ 50 m in diameter by the end of the eruption.

These successive eruptions, starting in November 2014, stopped following a collapse of the crater floor on May 3, 2015, with a felt earthquake, which was likely caused by the drain-back of the magma. The subsidence caused by this collapse reached 20–30 m in the southern half of the crater. The total volume of the subsidence was estimated to be 5.2×10^5 m^3 based on the observed differences between two photograph-based digital elevation models (DEMs) that were created in March and May 2015. After this collapse event, the high-temperature fumarolic activity at the southern inner wall of the crater apparently began to decrease to one-tenth of its original value (Cigolini et al. 2018). The heat discharge rate, which was 1–2 MW before and during the 2014–2015 eruptions, consequently reached 0.1–0.2 MW by the end of 2015. The thermal pathways beneath the crater were crushed during the collapse event.

Observation of infrasound waves and results

By the beginning of the 2014–2015 eruptions, we had previously established an infrasound network composed of five stations around the crater of Aso volcano (circles in Fig. 1c). Each station was equipped with a low-frequency microphone (Datamark SI104; flat response in 0.1–1000 Hz). The infrasound data at all the stations were recorded by GPS-time synchronized digitizers at a sampling frequency of 100 Hz. The KAE station, which was located only 300 m east of the crater center, was buried by ejected materials in early December 2014, i.e., shortly after the start of the eruptions. Thus, we can only use the KAE data obtained during the first 2 weeks of the eruptions.

The right-hand panels in Fig. 2 show the 10-min infrasound signals observed at ACM, the nearest station on the crater rim (Fig. 1c). It is evident that continuous and countless perturbations in pressure with a monochromatic nature were observed whenever any type of eruption (or no eruption) occurred at the vent. The corresponding power spectra showed a clear peak frequency of approximately 0.5–0.6 Hz (Fig. 4). The one-minute infrasound data recorded at all the stations show a high degree of correlation (Fig. 5a), excluding those recorded at KAE. These data reflect the clear monochromatic oscillations of the pressure data (dominant frequency of 0.68 Hz for 10-min data; 13:30–13:40 on December 15, 2015), with some amplitude modulation. Such monochromatic pressure oscillations appear to have been induced by, or occurred after, the incident wave packets (arrows in Fig. 5a). Another feature observed in the waveforms is that the observed pressure perturbations were derived from the crater as wave traces in Fig. 5a (from top to bottom), which are plotted in the order of increasing distance from the crater center.

To improve the signal-to-noise ratios of the signals and to elucidate the time evolution of their dominant frequency, we generated a stacked spectrogram using all the stations data that might have been measured at the distance of the ACM station from the crater center (Fig. 6a), assuming that the infrasound waves radiated outward from the crater center. Our assumption of the source location was validated as described in the next section. The infrasound waves at the stations at Aso volcano were obscured by windy conditions (McKee et al. 2017) due to the lack of vegetation around the crater. Contamination of the wind-derived pressure oscillations is easily recognized in the spectrogram of the infrasound data (Additional file 1), in which power concentrations ranged over a wide frequency band (0.01–10 Hz) during windy conditions. Therefore, we eliminated the data collected when the wind velocity observed at the JMA station (1.2 km WSW of the crater; a square in Fig. 1c) was $\geq$ 7.74 m/s, which is the average value of every 10-min record from November 2014 to May 2015. This threshold velocity of the wind was determined by taking a trial-and-error approach. As shown in Fig. 6a, these monochromatic infrasound signals were observed only during the period of the 2014–2015 eruption. The dominant frequency was not constant but instead fluctuated around 0.4–0.7 Hz over time. In late March and the middle of April, the frequency increased up to $\sim$ 1.5 Hz, caused by the intense Strombolian explosions and gas exhalations at the crater (Ishii et al. 2019).

The air pressure change recorded on the ground surface consists of three main components (Ichihara et al. 2012): the incident pressure wave itself and pressure changes due to vertical ground motion and wind. Here, we briefly describe how we verified the second contribution to our infrasound records. The third was not considered because we omitted the data during the strong wind conditions. A spectrogram of broadband seismic signals (vertical component) recorded at UMA (double circle in Fig. 1c; Guralp CMG-40T, 30 s–50 Hz) was also

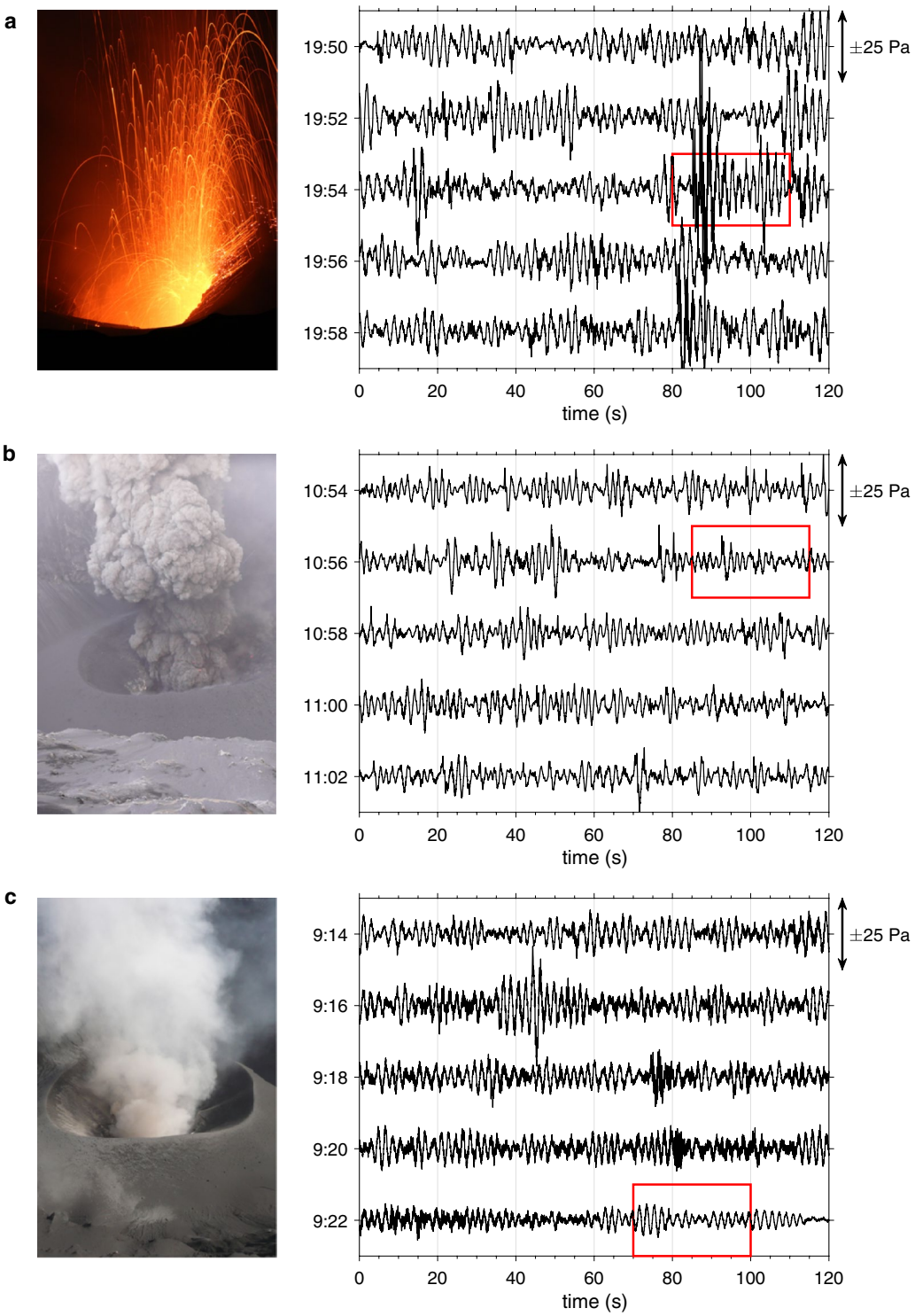

Fig. 2 Surficial phenomena and corresponding infrasound waveforms. Several types of surficial eruptive events (**a** Strombolian explosion; **b** ash ejection; and **c** emission of gas–steam mixtures) with their corresponding 10-min infrasound waveforms observed at ACM. All pictures in **a**–**c** were taken from the SW or SSW rim of the crater at 19:55 on April 18, 2015, 10:57 on January 13, 2015, and 9:23 on March 20, 2015, respectively. Timings of these snapshots were marked in the diagrams

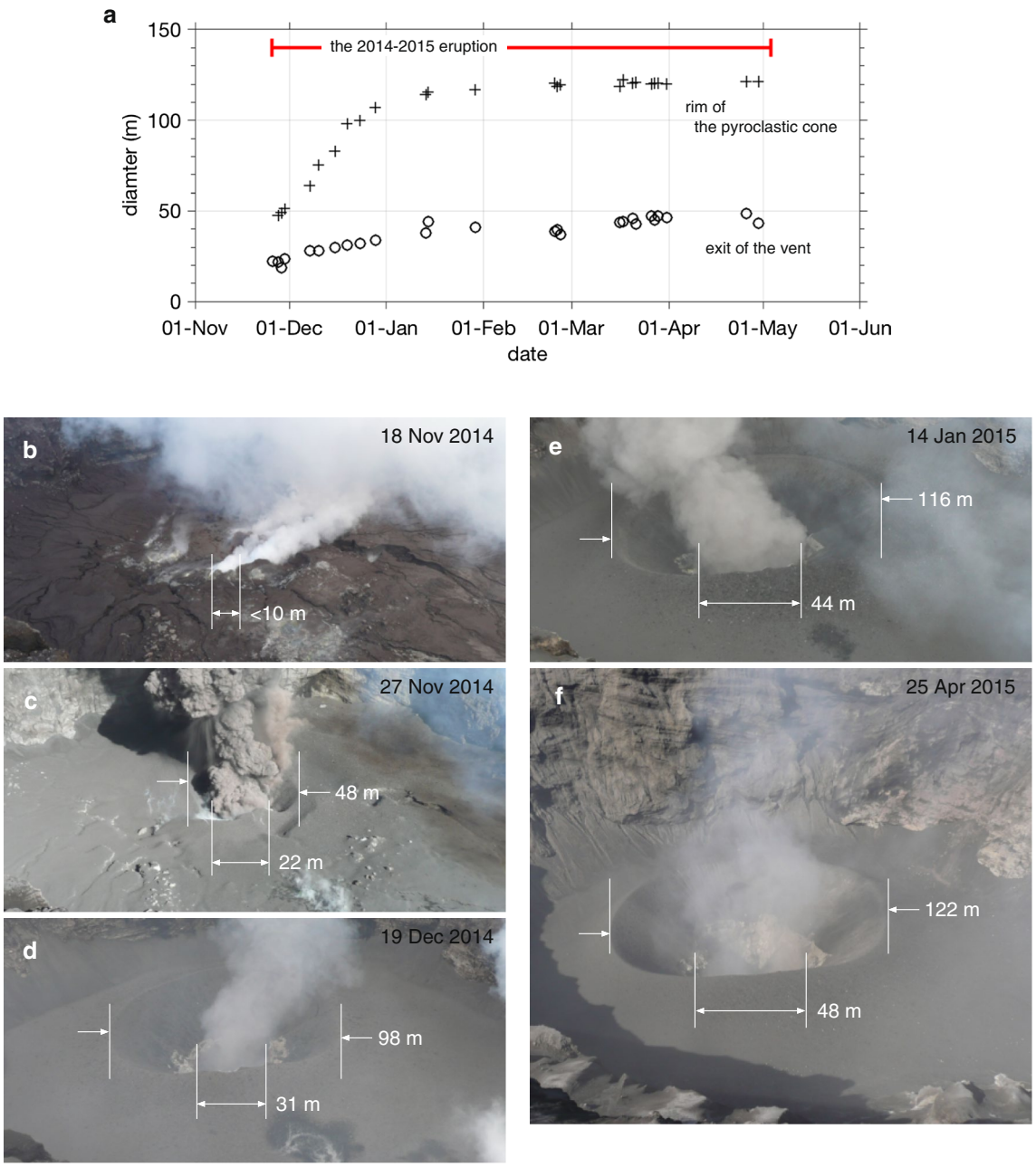

Fig. 3 Time evolution of sizes of pyroclastic cone and its vent. **a** Size of the pyroclastic cone built at the crater floor (crosses) and the exit of its vent (circles). Red bar indicates the period of the 2014–2015 eruption. **b–f** Photographs taken from the SSW crater rim showing growth of the pyroclastic cone and its vent

generated to compare the frequency features of the infrasound data to those of the seismic data (Fig. 6b). Many significant peaks occurred at < 0.6 Hz; however, there were no fluctuations over time, in contrast to the peak of the infrasound signals (0.4–0.7 Hz; Fig. 6a). The observed amplitude of the seismic records (10–100 μm/s) could contribute only $< 10^{-2}$ Pa to the infrasound. The value was too small to be observed in infrasound records (10–100 Pa; Fig. 2). These two findings indicate that the main component of the observed infrasound signals was the incident wave propagating in the air to the station.

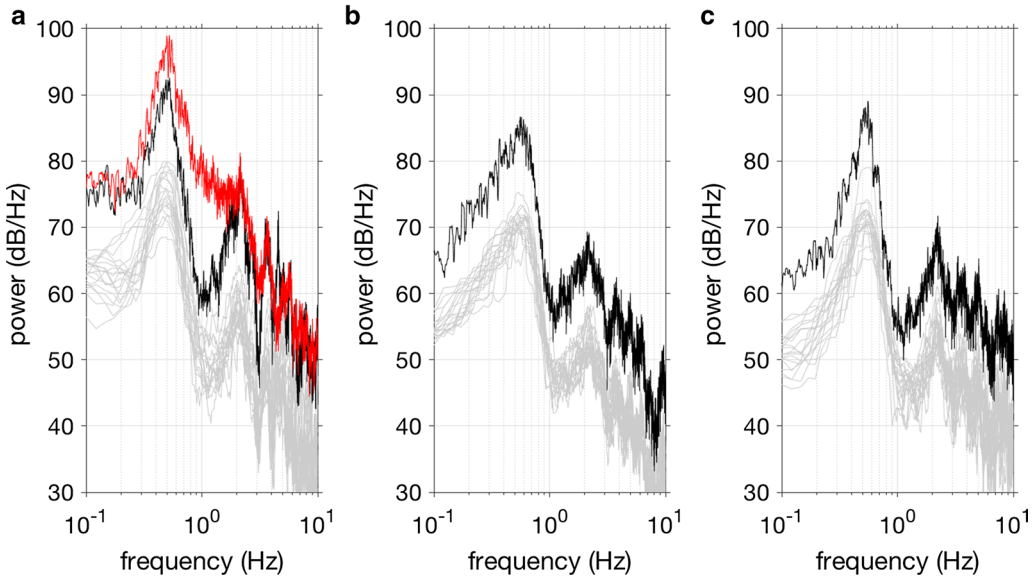

Fig. 4 Power spectra for Aso infrasound signals. Power spectra of a 10-min and 30-s records (black and gray lines, respectively) for the times of various surficial phenomena (**a** Strombolian explosion; **b** ash ejection; and **c** emission of gas-steam mixtures). Same data of Fig. 2 are used to calculate the spectra. Red line in **a** is data on March 25, 2015, when the intense Strombolian explosions and gas exhalations were observed

Source location of monochromatic infrasound waves

To estimate the source location of the monochromatic infrasound waves, a grid search method was applied following Yokoo et al. (2009). A root-mean-squared timing residual ϵ was calculated for each candidate grid of the source location:

$$\epsilon = \frac{1}{N_{\rm sp}} \sqrt{\sum \left(\Delta t^{\rm obs} - \Delta t^{\rm syn}\right)^2}, \tag{1}$$

where $N_{\rm sp}$ is the number of station pairs used to calculate a time lag (we chose times of $N_{\rm sp} \geq 4$ in this study); $\Delta t^{\rm obs}$ is the observed time lag of the monochromatic infrasound waves between two stations; and $\Delta t^{\rm syn}$ is the computed time lag based on the theoretical propagation of sound in the air. The latter time lag is also a function of the direction from a source location to the station with a given wind direction. The location determined by minimizing ϵ in Eq. (1) indicates the point from which the most intense signal at each time window is radiated.

The time lags $\Delta t^{\rm obs}$ observed between our spatially distinct stations (Fig. 1c) were calculated using a cross-correlation method. As shown in Fig. 5a, the waveforms observed at these stations are highly similar to each other. The monochromatic perturbation of the infrasound pressure continued for a long time, i.e., minutes to hours to days (Fig. 2). Therefore, we used every 10-min-long data point that was filtered by the 0.2–1.0 Hz band, which covers the dominant frequencies (Fig. 6a). We used only the data with the higher cross-correlation coefficient values ($R \geq 0.9$). The estimated time lags remained nearly constant throughout the entire period of investigation (Fig. 5b).

To estimate $\Delta t^{\rm syn}$, we first calculated the path length of the infrasound waves from each candidate source grid to each station. Candidate source locations (with 1 m spacing) were set on the ground surface within a circular area with a 500 m radius centered at the active crater (Fig. 7a). To accurately consider the topographic barriers in the 2-D profile, we used a 1-m-resolution DEM acquired by an airborne laser survey of the Geospatial Information Authority of Japan in 2012. Then, the travel time along the path from each grid to each station was calculated using the effective sound speed in the air $c_{\rm eff}$, which varies with both the air temperature $T_{\rm air}$ (K) and the wind velocity vector $\mathbf{v}$:

$$\begin{aligned} c_{\rm eff} &= c_{\rm air} + \mathbf{v} \cdot \mathbf{i} \\ &= \sqrt{\gamma R_0 T_{\rm air} / \overline{M}} + \mathbf{v} \cdot \mathbf{i}, \end{aligned} \tag{2}$$

where $c_{\rm air}$ is the air sound velocity and $\mathbf{i}$ is the unit vector for a given grid-to-sensor direction. $c_{\rm air}$ is also expressed using the ratio of specific heats γ (1.402), the universal gas constant R_0 (8.3144 J $\rm K^{-1}$ $\rm mol^{-1}$), $T_{\rm air}$, and the mean molar mass of the air $\overline{M}$ (28.966×10^{-3} kg $\rm mol^{-1}$). Over the entire observation period, we used actual temperature and wind data recorded every 10 min at the JMA

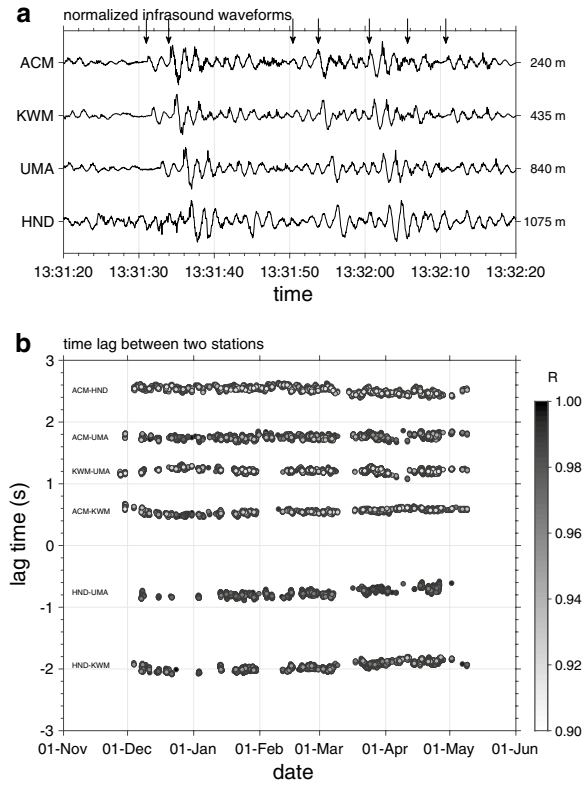

Fig. 5 Well-correlated infrasound waveforms between the stations. **a** Normalized one-minute infrasound waveforms recorded at four stations on December 15, 2015. Each trace from top to bottom is aligned in order of its horizontal distance from the crater center (annotated at the right; see Fig. 1). Arrows indicate beginning of monochromatic oscillations. **b** Results of cross-correlation analyses between all stations' data filtered by a 0.2–1.0 Hz pass-band. Only data with cross-correlation coefficients of $R \geq 0.9$ are plotted

station (Fig. 1c). These synthetic travel times were used to determine the Δt^{syn} values between the stations.

An example of a result estimating the source location is shown in Fig. 7a, which represents a case during the period of 13:30–13:40 on December 15, 2015. Some of the infrasound data (1 min) from this period are displayed in Fig. 5a. The source location of the monochromatic infrasound wave, as indicated by a cross in Fig. 7a, is definitely located at the actual vent position (Fig. 1c). The spatial distribution of the estimated ϵ values is somewhat elongated in the EW direction because we could not use data from the KAE station during this time period. For the entire 2014–2015 eruption, more than three thousand datasets (3115 10-min time data points) satisfied the threshold values of N_{sp} and R and were used to estimate the source location. All of the located infrasound sources are clustered around the active vent (Fig. 7b). The sources are located in a relatively narrow space, with the 1σ variances in the NS and EW directions being 8.6 m and 11.1 m, respectively. No apparent time evolution of the source locations could be identified, although the observed peak frequency changed over time (Fig. 6a).

Finite-difference time-domain computation of monochromatic infrasound waves

Trying to understand the conduit conditions responsible for the monochromatic infrasound waves observed during the 2014–2015 eruption at Aso volcano, we computed a 3-D pressure wavefield using a GPU-based finite-difference time-domain (FDTD) code (Kim and Lees 2014; Kim et al. 2015) that incorporates a rigid air–ground boundary and linear wave propagation. In this calculation, Gaussian-like pulses (the Blackman-Harris window; Harris 1978) with four different pulse widths of the pulse ($\tau = 0.16, 0.31, 0.78$, and 1.55 s; Fig. 8a) were used to represent impulsive pressure-time histories at the point source. This approach is equivalent to the use of a smoothed step function in time histories of a fluid flux, which might provide sustained pressure perturbations, as observed at Aso volcano (Fig. 2). We selected such a simple source waveform so that complex propagation effects (e.g., reflection and refraction) could be easily distinguished from the source effect. This pressure source was located at the bottom center of the conduit, similarly to the study of Morrissey and Chouet (1997), whose vertical length L varies from 0 to 200 m. We think it is inadequate to set the source in the midpoint of the air column inside the conduit for eruptions at Aso volcano. The radius of the conduit was fixed at 25 m at any depth (a simple straight pipe) reflecting the actual situation in late March (Figs. 2c, 3). The computation space was 2000 m $\times$ 2000 m $\times$ 2000 m, with a resolution of 2 m, in which the vertical space corresponded to altitudes ranging from 900 to 2900 m, analogous to the location of the crater at Aso volcano. Surrounding this computation space, we utilized perfectly matched layers with a depth of 50 m as the absorbing boundary layers. We adopted a time step of $\Delta t = 0.001$ s to satisfy the numerical stability condition (Wang 1996). The 1-D air sound speed and the 1-D density of the air were estimated based on the JMA station data (22:30 on March 25, 2015). The effects of wind and intrinsic attenuation in the air during the propagation of infrasound waves were not considered in these calculations.

We modeled infrasound radiation for both a half-space geometry and also with the topography provided by the DEM. This approach was adopted to distinguish first the effect of the conduit from complex observed signals. For example, even at stations on the crater rim at Erebus volcano, reflection effects from the crater topography were found in the infrasound signals

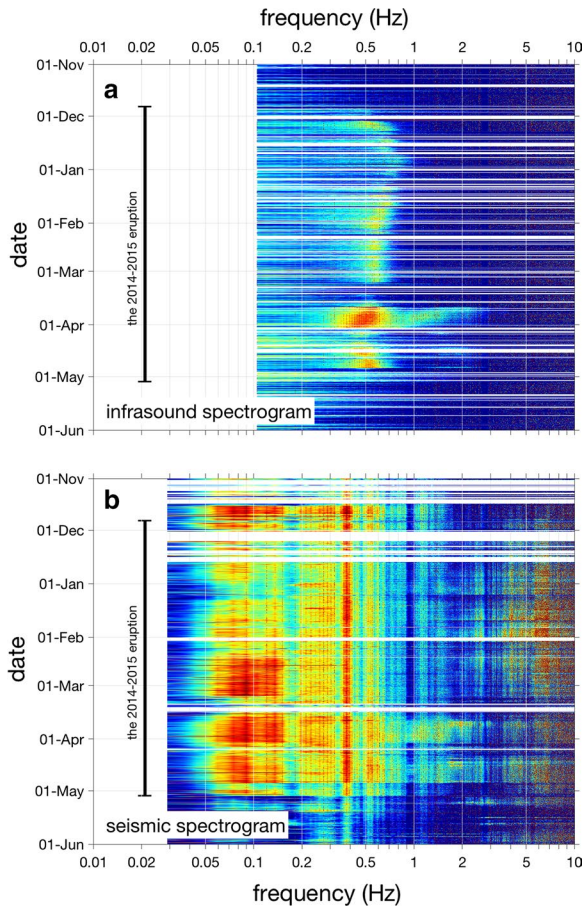

Fig. 6 Spectrograms of infrasound and seismic waves during the 2014–2015 eruption. **a** Seven-month stacked spectrogram of the infrasound record using reduced data of all the stations to ACM. Data obtained under windy conditions ($\geq$ 7.74 m/s at JMA; Fig. 1) are eliminated. Black bar on the left-hand side indicates the period of the 2014–2015 eruption. **b** Spectrogram of the broadband seismic record of the UMA station. Non-functional stations create data gaps

(Witsil and Johnson 2018). Figure 8b–f shows the simulated pressure distribution in the air at 3 s after the pressure initiation (a fixed pulse $\tau = 0.78$ s). These snapshots observed at different conduit lengths L highlight that the wavelengths of the pressure perturbation propagating toward the open space were not constant, even though the same initial pressure signal was used in the calculations. The computed waveforms at a location where the horizontal distance from the conduit is the same as that of the ACM station (Fig. 9a) showed systematic changes in their features with changes in L. At $L = 25$ m (top of Fig. 9a), the duration of the first positive phase of the waveform retained the differences in the original pulse widths at the wave source ($\tau = 0.16-1.55$ s). The subsequent negative phase, which was caused by reflection at the exit edge of the conduit (Kim and Lees 2011), also showed nearly the same length of pulse widths. However, such was not the case for $\tau = 1.55$ s. The reason why the reflected phase has a negative amplitude and the same width is that the open-exit reflection coefficient is nearly -1 when the wavelengths are much longer than the conduit radius (Stepanishen and Tougas 1993). The codas at all of the initial source conditions in a 25-m conduit are similar. In contrast, the longer L is (from top to bottom in Fig. 9a), the more significant the coda will be compared to the first positive signal, and the longer the wavelengths will be.

The wavelengths of the coda are strongly related to the lengths of the conduit L in which an initial pressure source was settled but are not related to the source width τ (Fig. 9a). To elucidate their relationships, the fundamental frequencies of the 10-s simulated waveforms observed at ACM were examined (Fig. 9c; Additional file 2). For example, for $\tau = 0.16$ s, the estimated fundamental frequency was nearly constant at approximately 2.3–2.5 Hz when the conduit length was short ($L \leq 10$ m). This frequency of ~ 2 Hz gradually decreased to ~ 0.37 Hz at $L = 200$ m. Under other initial conditions ($\tau = 0.31, 0.78$, and 1.55 s), the estimated fundamental frequencies of the waveforms showed the same change curves. We confirmed that the coda frequency was predominantly controlled by the conduit length L even under different initial τ values, as expected.

Following Kinsler et al. (1999), the normal mode f_0 of an open-end pipe (the other end is closed) with the end correction (flanged) is described by

$$f_0 = \frac{c_{\mathrm{air}}}{4(L + 8a/3\pi)}, \tag{3}$$

where c_{air} is the air sound speed in the pipe, L is the pipe length, and a is the pipe radius. To achieve a straightforward interpretation of the condition of the space inside the conduit, we fixed the values of c_{air} and a to 338 m/s and 25 m, respectively, which are the same as the values used in the FDTD calculation. The red line in Fig. 9c shows the theoretical shift in the frequency f_0 with the conduit lengths L. We identified no significant differences between this frequency and the change curve of the fundamental frequencies of the simulated pressure waveforms described in the previous paragraph. This result suggests that the coda in our simulated waveforms was undoubtedly a resonant tone of the conduit that was caused by the oscillating pressure waves in the conduit.

We then incorporated topographic data from Aso volcano into the FDTD calculation. The DEM used for the calculation was established using two datasets acquired in different years. The dataset used for the area outside

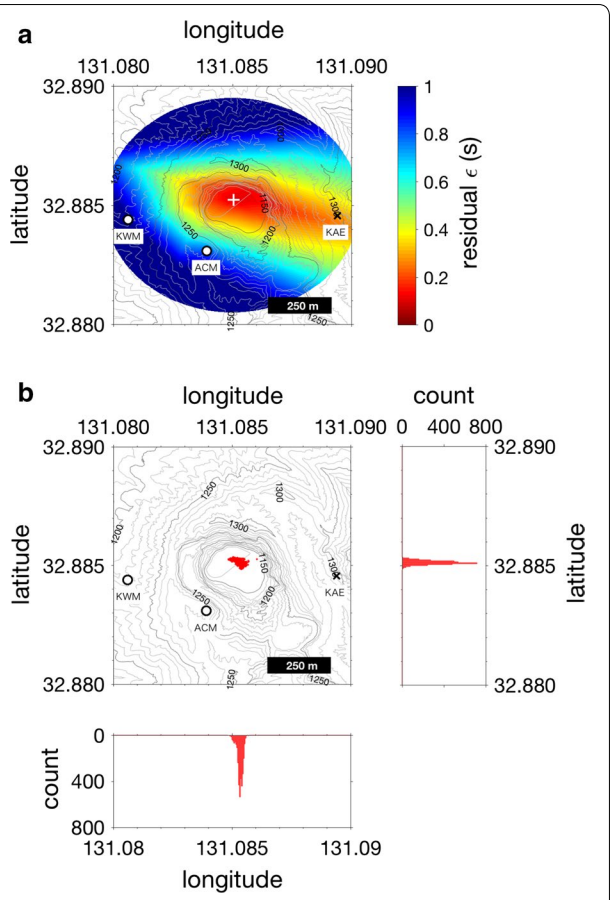

Fig. 7 Source location of monochromatic infrasound waves. **a** Spatial distribution of the timing residual ϵ for 10-min data during 13:30–13:40 on December 15, 2015. White cross at the crater center shows a location with the minimum value ($\epsilon = 0.10$ s). **b** Source location of the 10-min infrasound records during the entire eruption period (N = 3115)

the crater was the 2012 DEM, which was the same as that used to estimate the source locations of the infrasound waves. The other dataset (inside the crater) was newly created from datasets based on our ground-based and aerial photogrammetry surveys, which were conducted on March 26 and 27, 2015, respectively. We merged both the 2012 and 2015 DEMs and decimated the new one to a resolution of 2 m. All other conditions in the numerical calculations, such as τ and L, were not changed.

The simulated waveforms obtained using the volcano DEM and their fundamental frequencies are shown in Fig. 9b, d. Compared to the waveforms obtained under no-topography conditions (Fig. 9a), the waveforms under the actual topography were greatly distorted due to the reflections and diffractions occurring during the wave propagation. For example, at $L = 25$ m (top in Fig. 9b), all of the waveforms had a coda with a much longer duration. At $\tau = 1.55$ s (the bottom trace of the four waveforms), the negative phase following the first positive phase became conspicuous. As L increased, the distortions of the first positive phase became more noticeable, especially in the minor secondary peak on the right shoulder. The codas were still pronounced, similarly to those in the no-topography calculations; however, the peak frequencies of the 10-s waveforms at $L \geq 30$ m were ~ 15% smaller than the theoretical f_0 values obtained from Eq. (3) (red solid and broken lines, respectively, in Fig. 9d). This decrease in f_0 was also due to the effect of topography during wave propagation. Another topographic effect was observed in the fundamental frequencies for conditions involving a shorter conduit, approximately 0.4, 1.3, and 2.1 Hz (Fig. 9d and Additional file 2), although the effect was inconspicuous compared to that in the cases of a longer conduit. However, we argue that any source time function could not generate the different frequency contents of the coda, similarly to the calculations performed without topography. The main feature of the observed waveforms as low-frequency pressure oscillations was produced only by the air resonance in the conduit.

Constraint on conduit size from observed infrasound waveforms

Based on our FDTD calculations described in the previous section, we invoke a simple model of the monochromatic pressure perturbation of the infrasound wave records during the 2014–2015 eruption at Aso volcano. The observed infrasound waves could be explained as a resonance of the air within the top portion of the conduit above the magma free surface. The concept is similar to the models proposed for infrasound coda observed at Etna (Spina et al. 2015), Cotopaxi (Johnson et al. 2018b), Villarrica (Richardson et al. 2014), and Erebus volcanoes (Witsil and Johnson 2018). This idea suggests that we have the potential to constrain both the size of the conduit and the source time function for the radiation of the infrasound signal. We used a sample case on March 25, 2015, to demonstrate this procedure. During this simulation, we made two assumptions: (1) the shape of the conduit was a pipe with a radius of 25 m, as we observed (Fig. 3), that the conduit does not change in size with depth, and (2) the conduit was filled with air whose temperature is the same as that of the surrounding air estimated from the JMA data. Although we did not consider volcanic gas species, temperatures similar to those in the air condition were concluded in the Cotopaxi's case (Johnson et al. 2018b). This analysis comprised two steps. During the first process, the peak frequency of the monochromatic infrasound waves was examined to determine the length of the conduit. Then, we compared the waveforms of the first positive–negative phases between the

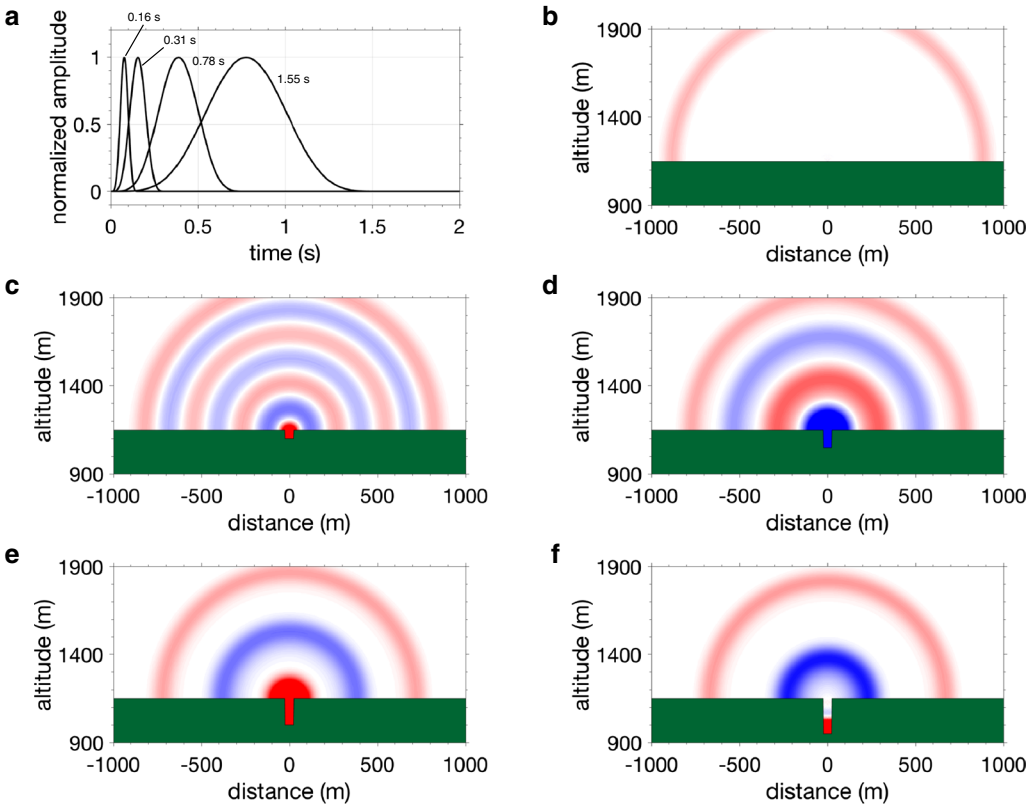

Fig. 8 Snapshots of the pressure distribution with different conduit lengths. **a** Simple source time functions used in our FDTD calculations. **b**–**f** Snapshots of pressure distribution at 3.0 s after the initiation of the 0.78-s width pulse. The conduit lengths are 0 m, 50 m, 100 m, 150 m, and 200 m in **b**–**f** respectively. Red and blue colors represent positive and negative pressures, respectively

observed and simulated infrasound waves to constrain the source time function occurring inside the conduit.

Over the period of 22:23:00–22:23:10 on the day when intense eruption activities were marked, the peak frequency of the observed infrasound records was 0.51–0.52 Hz (Figs. 4a, 6a). Based on the results of the FDTD calculation including the actual topography, in which f_0 showed a $\sim$ 15% decrease from its original value on a simple pipe resonance predicted by Eq. (3) (Fig. 9d), the conduit length L could be estimated as $\sim$ 118 m using the peak frequency. Then, we simulated the infrasound wave that would be observed at the ACM station if the 118-m-long conduit was located at the eruptive vent. In this calculation, we used τ values ranging from 0.16 s to 1.55 s. A change in the source pulse width τ could gradually distort the waveform of the first positive phase (Fig 9b). We compared a set of the first positive and negative phases obtained from the observed and simulated infrasound waves (O and S, respectively) using the residuals; $\sum \left((O^2 - S^2)/O^2 \right)$. Figure 10 shows a result of the best-correlated waveforms obtained when a pulse width of $\tau = 0.70$ s was given at the source. The similarities between not only the first pulses of the waveforms but also the entire shapes of the waveforms were notable because we had already matched the peak frequency of the coda during the first step. For this case, by time-integrating the 0.70-s width pressure pulse (6300 Pa), a smoothed step function of the mass flow rate from 0 kg/s to 3.9×10^4 kg/s, and therefore, a step in the volume rate from 0 to 4.0×10^4 m^3/s considering the air density of 1.10 kg/m^3, could be deduced at the source. Assuming that the degassing constantly occurs over the cross-sectional area of the conduit (2.0×10^3 m^2), we calculated the exit velocity of the gas to be 18 m/s. This velocity coincided with the lower range of a gas thrust recorded during Strombolian explosive dynamics (Patrick et al. 2007; Delle Donne and Ripepe 2012). However, this example was a much larger event among those of the entire 2014–2015 eruption, and in most cases, the observed signals might show a velocity of gas exhalation that is more than one order of magnitude smaller by comparison (Figs. 2, 4). This finding suggests that most of these events could be reflected by the dynamics of the buoyant type of eruptions involving much slower

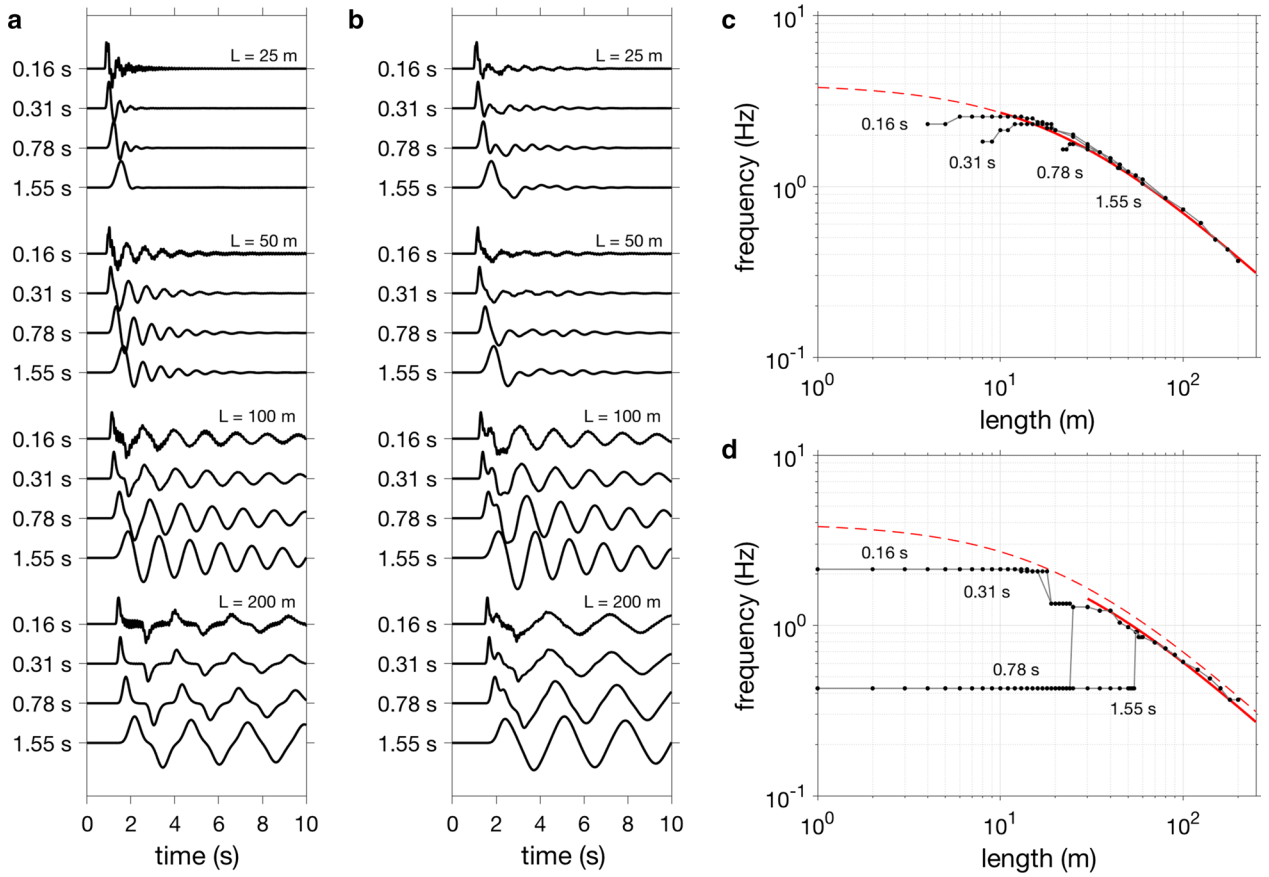

Fig. 9 Results of FDTD numerical calculation. **a** Simulated waveforms to be observed at ACM without consideration of topography (see Fig. 8b–f). The results obtained using four different pulse widths of the source (Fig. 8a) and four conduit lengths are shown. Radius of the conduit is fixed as 25 m for all cases. **b** Simulated waveforms of the FDTD calculation including the topographic data of Aso volcano. **c** The peak frequency of the 10-s synthetic waveforms as shown in **a** for the no-topography calculation. The observed frequencies for the > 10 m conduit lengths are fit to theoretical values estimated using Eq. (3) (red line). **d** The frequencies of the waveforms in **b** using the Aso DEM are 15% smaller (red line; > 30 m length) than the theoretical expectation at a simple pipe with a flat topography (broken red line; same line in **c**)

velocities (Patrick et al. 2007). A slight difference in the decay rate of the amplitude (the quality factor Q) in the coda part was observed (Fig. 10b). The calculated waveform had a higher Q value than that of the observed waveform. Johnson et al. (2018a, b) showed that a conduit's geometry, especially its radius, influences the Q values. The misfit in the coda part might be much improved by using more adequate parameters that we did not consider in this analysis.

We successfully estimated the length of the conduit and the source time function for the observed signals of the monochromatic infrasound waves. However, it was assumed that the conduit was a simple pipe filled with the air of an ordinary temperature, which reflects a potential limitation of our method. The source time function we used in the calculation, the Blackman-Harris function for the pressure pulse, might be another reason for this limitation. If we want to interpret much more realistic source conditions associated with the infrasound wave records, we need to consider the effects of other parameters that we fixed in the FDTD calculation. Some examples of these parameters include changes in the sound velocity c_{air} and the size (conduit radius, a) and shape of the conduit (from a straight pipe to a conical pipe). The sound velocity can be modified with a fraction of mixtures with gas and magma fragments (e.g., Morrissey and Chouet 2001). In fact, various surficial phenomena were observed at Aso volcano when we observed the same ~ 0.5 Hz monochromatic infrasound tremor (Figs. 2, 4). An infrasound coda with 0.4-Hz peak frequency was also observed during the fire-fountaining at Etna volcano (Ulivieri et al. 2013). This observation indicates that the fixed sound velocity may not be appropriate. In Etna's case, the possibility of interference with the resonance process itself by the sustained magmatic flux might be investigated. The differences in the peak frequency of

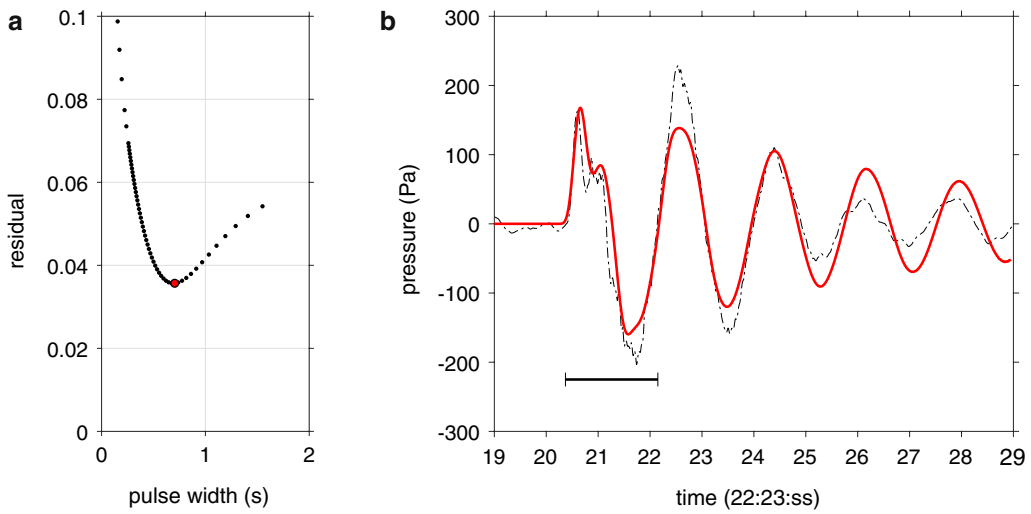

Fig. 10 Comparison of synthetic and observed infrasound waveforms. **a** Residual between synthetic and observed infrasound waveforms (only for the first one cycle as indicated by a horizontal bar in **b**; at 22:23:20 on March 25, 2015). The minimum value (red point) is marked on the simulated waveform using a 0.70-s width pulse inside a 118-m-long conduit. **b** Waveform fits between synthetic and observed infrasound waveforms (red solid and black broken lines, respectively)

the pressure perturbation caused by changes in these parameters were examined quantitatively using Eq. (3) and based on the work of Ayers et al. (1985). Figure 11 shows that all of these parameters independently affect the fundamental resonant frequency of a pipe. In particular, the sound velocity inside the pipe has a significant effect on the uncertainty of the estimation of the conduit length. Various combinations of parameters could be used to generate the observed frequencies of the infrasound waves used above, i.e., 0.51–0.52 Hz. This finding suggests that the conduit length we estimated should be further validated from another perspective, such as based on the time difference between the arrivals of infrasound and seismic waves (e.g., Richardson et al. 2014). The time difference is certainly relevant to both the conduit length and the sound velocity within the conduit. Therefore, a reasonable range of both parameters satisfying the observed time difference of the data should be evaluated using a method based on the probability density functions (Ishii et al. 2019). The joint analysis of the infrasound-based estimation performed in this study and an estimation performed using this type of seismo-acoustic method (Ishii et al. 2019) may be a robust tool with which to constrain the local topography of the vent. This approach could lead to a better comprehensive investigation of the conduit parameters to understand why the peak frequency changed over time during the eruption period (Fig. 6a). We also found that infrasound waveform inversions (Kim et al. 2015) do not necessarily provide an actual source time history unless the conduit geometry and its associated resonant tones are incorporated into the inversion. The accurate response function of the conduit should be assessed in cases of small-scale eruptions, such as Strombolian explosions. Otherwise, an incorrect source time function (i.e., incorrect mass fluxes) may be deduced, thus leading to incorrect interpretations of eruption processes.

Summary

During the 2014–2015 eruptions at Aso volcano in Japan, we successfully observed monochromatic infrasound tremor at stations around the crater. The peak frequency of the tremor was 0.4–0.7 Hz, which gradually changed over time. However, these infrasound signals were associated not only with Strombolian eruptions or ash ventings but also with emissions of gas–steam mixtures. This result suggests that the monochromatic infrasound waves we observed were mainly caused by the air resonance inside the conduit. Such resonance may have been produced by an incident pressure oscillation at the base of the conduit, such as that caused by a degassing process. We determined whether this process could occur at Aso based on a numerical calculation using the finite-difference time-domain method with accurate topography data with a resolution of 2 m. The results of this calculation indicated that the peak frequency of the monochromatic infrasound waves could be accounted for by the length of the conduit, regardless of variations in the source time function. Assuming a series of conditions on a day in March 2015, we also reproduced a waveform of the observed monochromatic infrasound signals. The results suggest that the gas exhalation with a gas velocity

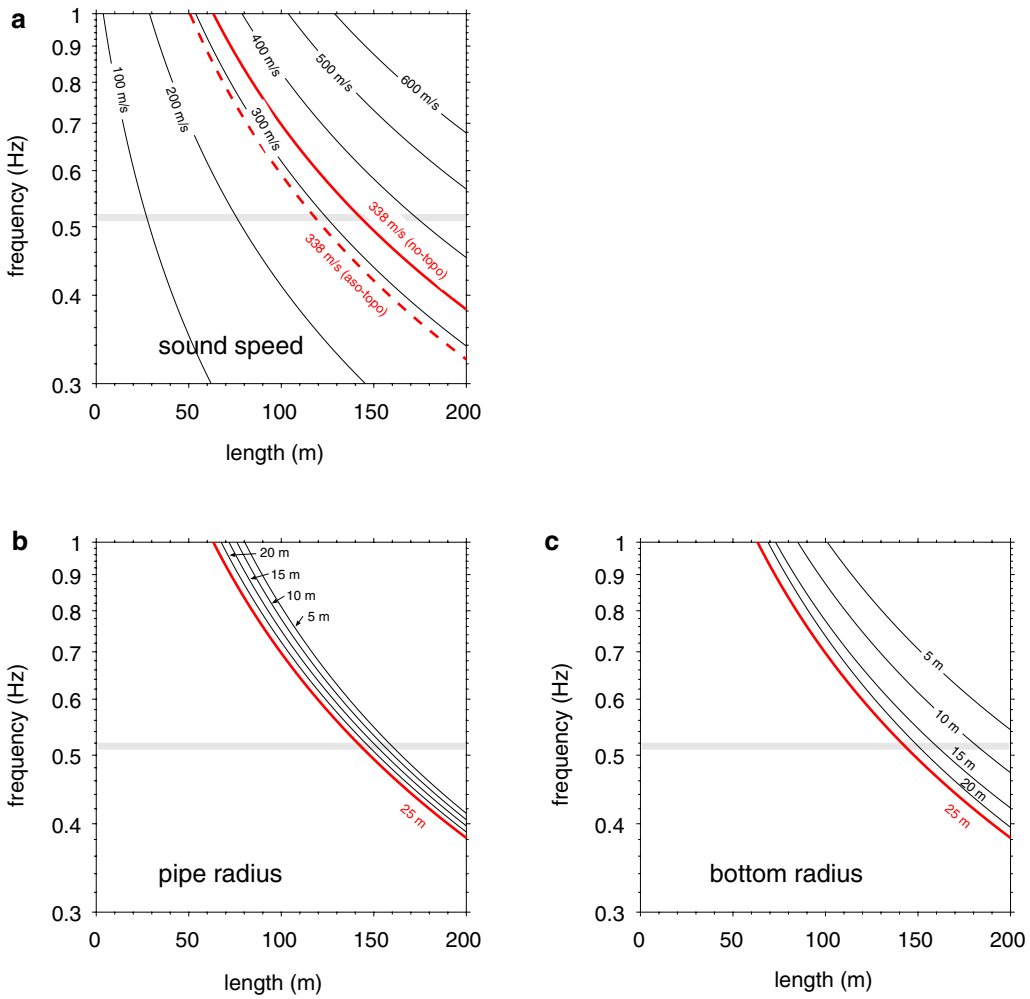

Fig. 11 Length dependence on the fundamental resonant frequency of a pipe. **a** Relationship between pipe length (L) and resonant frequency (f_0) with variable sound speed inside the pipe (c_{air}; 100–600 m/s) calculated using Eq. (3) with a fixed radius of the pipe ($a = 25$ m). Red solid and dashed lines show the velocity of 338 m/s used in our FDTD calculations (without and with topographic data, respectively). The peak frequency of the observed infrasound records is shown by a gray horizontal bar (0.51–0.52 Hz at 22:23:00–22:23:10 on March 25, 2015). **b** Dependency of variable size of pipe radius (a). The red line is the same as that in **a**: $a = 25$ m, $c_{air} = 338$ m/s, and without topographic conditions. **c** Effect of pipe geometry from a simple straight pipe to a conical pipe. The bottom radius of the pipe changes from 25 m (red line) to 5 m, whereas the radius of the other side (top portion) is fixed at 25 m (a)

of 18 m/s occurred at 120 m depth in the conduit. However, further (joint) analysis using seismic data is required to more accurately constrain the conduit parameters, such as the conduit's length and the sound speed of the air inside it.

Authors' contributions

AY performed all the analyses in this study and led the interpretation of the results. KI and TO provided critical comments for this study and supported the observations. TO made DEMs of the crater. KK set up the numerical code of infrasound propagation. All authors read and approved the final manuscript.

Author details

[1] Aso Volcanological Laboratory, Institute for Geothermal Sciences, Kyoto University, 3028 Sakanashi, Aso, Kumamoto 869-2611, Japan. [2] Department of Geophysics, Graduate School of Science, Kyoto University, Kitashirakawa Oiawke-cho, Kyoto 606–8502, Japan. [3] Atmosphere, Earth, and Energy Division, Lawrence Livermore National Laboratory, 7000 East Avenue, L-414, Livermore, CA 94550, USA.

Acknowledgements

We are grateful to all staff of the Aso Volcanological Laboratory for their warm support of our study. Insightful comments and suggestions from J. Johnson, M. Ripepe, and V. Acocella greatly improved the manuscript. The Geospatial Information Authority of Japan provided the 2012 DEM of the Aso volcano. We collaborated with T. Kazama to make the DEM on March 2015.

Competing interests

The authors declare that they have no competing interests.

Availability of data and materials

The data that support the findings of the present study are available from the corresponding author upon request.

Funding
The present study was financially supported by Ministry of Education, Culture, Sports, Science and Technology of Japan under its Earthquake and Volcano Hazards Observation and Research Program, the JSPS-KAKENHI 25870352 to AY, and H29-ISHIZUE from Kyoto University to AY.

Publisher's Note

Received: 30 August 2018 Accepted: 24 January 2019
Published online: 31 January 2019

References

Ayers RD, Eliason L, Mahgerefteh D (1985) The conical bore in musical acoustics. Am J Phys 53:528–537. https://doi.org/10.1119/1.14233

Cigolini C, Coppola D, Yokoo A, Laiolo M (2018) The thermal signature of Aso Volcano during unrest episodes detected from space and ground-based measurements. Earth Planets Space 70:67. https://doi.org/10.1186/s40623-018-0831-7

Delle Donne D, Ripepe M (2012) High-frame rate thermal imagery of Strombolian explosions: implications for explosive and infrasonic source dynamics. J Geophys Res 117:B09206. https://doi.org/10.1029/2011JB008987

Fee D, Matoza RS (2013) An overview of volcano infrasound: from Hawaiian to Plinian, local to global. J Volcanol Geotherm Res 249:123–139. https://doi.org/10.1016/j.jvolgeores.2012.09.002

Fee D, Garcés M, Patrick M, Chouet B, Dawson P, Swanson D (2010) Infrasonic harmonic tremor and degassing bursts from Halema'uma'u Crater, Kilauea Volcano, Hawaii. J Geophys Res 115:B11316. https://doi.org/10.1029/2010JB007642

Fee D, Haney MM, Matoza RS, Eaton ARV, Cervelli P, Schneider DJ, Iezzi AM (2017a) Volcanic tremor and plume height hysteresis from Pavlof Volcano, Alaska. Science 355:aah6108. https://doi.org/10.1126/science.aah6108

Fee D, Izbekov P, Kim K, Yokoo A, Lopez T, Prata F, Kazahaya R, Nakamichi H, Iguch M (2017b) Eruption mass estimation using infrasound waveform inversion and ash and gas measurements: evaluation at Sakurajima Volcano, Japan. Earth Planet Sci Lett 480:42–52. https://doi.org/10.1016/j.epsl.2017.09.043

Goto A, Johnson JB (2011) Monotonic infrasound and Helmholtz resonance at Volcan Villarrica (Chile). Geophys Res Lett 38:L06301. https://doi.org/10.1029/2011GL046858

Harris FJ (1978) On the use of windows for harmonic analysis with the discrete Fourier transform. Proc IEEE 66(1):51–83. https://doi.org/10.1109/PROC.1978.10837

Ichihara M, Takeo M, Yokoo A, Oikawa J, Ohminato T (2012) Monitoring volcanic activity using correlation patterns between infrasound and ground motion. Geophys Res Lett 39(4):L04304. https://doi.org/10.1029/2011GL050542

Ishii K, Yokoo A, Kagiyama T, Ohkura T, Yoshikawa S, Inoue H (2019) Gas flow dynamics in the conduit of Strombolian explosions inferred from seismo-acoustic observations at Aso volcano, Japan. Earth Planets Space. https://doi.org/10.1186/s40623-019-0992-z

Johnson J, Watson LM, Palma JL, Dunham EM, Anderson JF (2018a) Forecasting the eruption of an open-vent volcano using resonant infrasound tones. Geophys Res Lett 45:2213–2220. https://doi.org/10.1002/2017GL076506

Johnson JB, Ripepe M (2011) Volcano infrasound: a review. J Volcanol Geotherm Res 206:61–69. https://doi.org/10.1016/j.jvolgeores.2011.06.006

Johnson JB, Ruiz MC, Ortiz HD, Watson LM, Viracucha G, Ramon P, Almeida M (2018b) Infrasound tornillos produced by Volcán Cotopaxi's deep crater. Geophys Res Lett 45:5436–5444. https://doi.org/10.1029/2018GL077766

Kim K, Lees JM (2011) Finite-difference time-domain modeling of transient infrasonic wavefields excited by volcanic explosions. Geophys Res Lett 38:L06804. https://doi.org/10.1029/2010GL046615

Kim K, Lees JM (2014) Local volcano infrasound and source localization investigated by 3D simulation. Seismol Res Lett 85(6):1177–1186. https://doi.org/10.1785/0220140029

Kim K, Fee D, Yokoo A, Lees JM (2015) Acoustic source inversion to estimate volume flux from volcanic explosions. Geophys Res Lett 42(13):5243–5429. https://doi.org/10.1002/2015GL064466

Kinsler LE, Frey AR, Coppens AB, Sanders JV (1999) Fundamentals of acoustics, 4th edn. Wiley, New York

Matoza R, Fee D, Garcés M, Seiner J, Ramón P, Hedlin M (2009) Infrasonic jet noise from volcanic eruptions. Geophys Res Lett 36:L08303. https://doi.org/10.1029/2008GL036486

McKee K, Fee D, Yokoo A, Matoza R, Kim K (2017) Analysis of gas jetting and fumarole acoustics at Aso Volcano, Japan. J Volcanol Geotherm Res 340(4):16–29. https://doi.org/10.1016/j.jvolgeores.2017.03.029

McNutt SR, Thompson G, Johnson J, De Angelis S, Fee D (2016) Seismic and infrasonic monitoring. In: Sigurdsson H, Houghton B, McNutt SR, Rymer H, Stix J (eds) The encyclopedia of volcanoes, 2nd edn. Elsevier Inc., London, pp 1071–1099. https://doi.org/10.1016/B978-0-12-385938-9.00063-8

Miyabuchi Y, Iizuka Y, Hara C, Yokoo A, Ohkura T (2018) The September 14, 2015 phreatomagmatic eruption of Nakadake first crater, Aso Volcano, Japan: eruption sequence inferred from ballistic, pyroclastic density current and fallout deposits. J Volcanol Geotherm Res 351:41–56. https://doi.org/10.1016/j.jvolgeores.2017.12.009

Morrissey MM, Chouet BA (1997) Burst conditions of explosive volcanic eruptions recorded on microbarograph. Science 275:1290–1293. https://doi.org/10.1126/science.275.5304.1290

Morrissey MM, Chouet BA (2001) Trends in long-period seismicity related to magmatic fluid compositions. J Volcanol Geotherm Res 108:265–281. https://doi.org/10.1016/S0377-0273(00)00290-0

Ono K, Watanabe K, Hoshizumi H, Ikebe S (1995) Ash eruption of the Nakadake crater, Aso volcano, southwestern Japan. J Volcanol Geotherm Res 66:137–148. https://doi.org/10.1016/0377-0273(94)00061-K

Patrick MR, Harris AJL, Ripepe M, Dehn J, Rothery DA, Calvari S (2007) Strombolian explosive styles and source conditions: insights from thermal (flir) video. Bull Volcanol 69:769–784. https://doi.org/10.1007/s00445-006-0107-0

Richardson JP, Waite GP, Palma JL (2014) Varying seismic-acoustic properties of the fluctuating lava lake at Villarrica volcano, Chile. J Geophys Res 119:5560–5573. https://doi.org/10.1002/2014JB011002

Ripepe M, Marchetti E, Bonadonna C, Harris AJL, Pioli L, Ulivieri G (2010) Monochromatic infrasonic tremor driven by persistent degassing and convection at Villarrica Volcano, Chile. Geophys Res Lett 37:L15303. https://doi.org/10.1029/2010GL043516

Spina L, Cannata A, Privitera E, Vergniolle S, Ferlito C, Gresta S, Montalto P, Sciotto M (2015) Insights into Mt. Etna's shallow plumbing system from the analysis of infrasound signals, August 2007–December 2009. Pure Appl Geophys 172:473–490. https://doi.org/10.1007/s00024-014-0884-x

Stepanishen P, Tougas RA Jr (1993) Transient acoustic pressure radiated from a finite duct. J Acoust Soc Am 93(6):3074–3084. https://doi.org/10.1121/1.405739

Ulivieri G, Ripepe M, Marchetti E (2013) Infrasound reveals transition to oscillatory discharge regime during lava fountaining: implication for early warning. Geophys Res Lett 40:3008–3013. https://doi.org/10.1002/grl.50592

Wang S (1996) Finite-difference time domain approach to underwater acoustic scattering problems. J Acoust Soc Am 99(4):1924–1931. https://doi.org/10.1121/1.415375

Witsil AJC, Johnson JB (2018) Infrasound explosion and coda signal investigated with joint analysis of video at Mount Erebus, Antarctica. J Volcanol Geotherm Res 357:306–320. https://doi.org/10.1016/j.jvolgeores.2018.05.002

Yokoo A, Miyabuchi Y (2015) Eruption at the Nakadake 1st crater of Aso volcano started in November 2014. Bull Volcanol Soc Jpn 60(2):275–278. https://doi.org/10.18940/kazan.60.2_275

Yokoo A, Tameguri T, Iguchi M, Ishihara K (2008) Sequence and characteristics of the 2007 eruption at Showa crater of Sakurajima volcano. Ann Disas Prev Res Inst Kyoto Univ 51B:273–276

Yokoo A, Tameguri T, Iguchi M (2009) Swelling of a lava plug associated with a Vulcanian eruption at Sakurajima Volcano, Japan, as revealed by infrasound record: case study of the eruption on January 2, 2007. Bull Volcanol 71(6):619–630. https://doi.org/10.1007/s00445-008-0247-5